Conf-950226--23

LA-UR-95-534

Title: TIME-DEPENDENT MODEL FOR VERTICAL-CAVITY
SURFACE-EMITTING LASER

Author(s): L. Thode
G. Csanak
R. Hotchkiss
C. Snell

Submitted to: SPIE
San Jose, CA
February 1995

MASTER

RECEIVED
MAR 10 1995
DISTI

Los Alamos
NATIONAL LABORATORY

DISTRIBUTION OF THIS DOCUMENT IS UNLIMITED

DISCLAIMER

Portions of this document may be illegible in electronic image products. Images are produced from the best available original document.

Time-dependent model for vertical-cavity surface-emitting laser

L. Thode, G. Csanak, R. Hotchkiss, C. Snell

Los Alamos National Laboratory, Los Alamos, NM

M. Campbell

PASTDCO, Albuquerque, NM

ABSTRACT

Two models have been developed to simulate a vertical-cavity surface-emitting laser (VCSEL). The first model is a two-dimensional time-dependent solution of Maxwell's equations, with frequency-independent bulk dielectric and absorption coefficients. These bulk coefficients depend upon the material, lattice temperature, and carrier concentration. This field model is coupled with a frequency-dependent gain model that describes the quantum well regions in the time domain. Treatment of frequency-dependent media in a finite-difference time-domain code is computationally intensive. On the other hand, because the volume of the active region is small relative to the volume of the distributed laser cavity, the computational overhead is reasonable. A semi-empirical transport model is used to describe the bulk transport, which drives the quantum well transport. In addition, the semi-empirical model provides a spatial distribution for the lattice temperature and carrier concentrations. The second model is a three-dimensional solution of Maxwell's equations. The three-dimensional model can be used for cold-cavity calculations. The two-dimensional code generates the dielectric and absorption coefficients assuming azimuthal symmetry, providing the initial conditions for the three-dimensional calculation.

1. INTRODUCTION

The VCSEL exhibits a strong variation in the index of refraction along the direction of propagation. As such, the propagation direction must be included to accurately simulate a VCSEL. Consequently, the VCSEL requires a three-dimensional field simulation to obtain an accurate intensity distribution within the laser cavity. Moreover, since the strong variation in the index of refraction occurs with a length scale less than the laser wavelength, most of the standard laser approximations are not valid for this device. Thus, Maxwell's equations must be solved in a complicated geometry with various boundary conditions.

Our goal was to develop a fairly complete quantum well laser model that attempts to take into account all important physical effects. As a result, the VCSEL laser model must combine three coupled systems: Maxwell's equations, the optical Bloch equations (OBE), and bulk transport equations. Because of the computational overhead associated with a full three-dimensional code, we first developed a two-dimensional model as a testbed for a three-dimensional model. Besides acting as a testbed, the two-dimensional code should be useful as a preliminary scoping code. As a result, we have compared the two-dimensional code against a reference VCSEL device.[1]

The reference VCSEL was designed to operate at 9800 Å. However, just above threshold, the device actually operates at 9335 Å. As the injection current increases, the mean wavelength of the device increases, and the number of excited transverse modes increases from one to a maximum of six.

The transverse mode separation remains about 10 Å, independent of the injection current. The intensity pattern starts as a Gaussian-like distribution, evolves into a donut-like pattern, to higher $\ell \neq 0$ modes, and then into filaments.

A deficiency in two-dimensional model comparison with the reference design is the lack of a bulk transport model. The original intent was to use a heterostructure version of PISCES that would provide the bulk solution for the electron concentration, hole concentration, and lattice temperature.[2] Since the transport and Maxwell-OBE algorithms are solved on a somewhat different mesh, a transformation scheme based upon the gather-scatter algorithms used in particle-in-cell plasma simulation codes was constructed to connect transport and field-gain algorithms. The basic assumption behind the transformation was that the electron and hole concentrations would be smooth functions in space. Unfortunately, this assumption proved to be incorrect, and the integration of the transport model to the field-gain model failed. As a result, the field-gain code utilizes a semi-empirical solution to connect the electron and hole concentrations with the lattice temperature. The longitudinal and transverse profiles for the concentrations and temperature are approximations gleaned from the PISCES solutions. This relationship clearly impacts the details of the simulation, but the two-dimensional simulation was expected to predict the basic trends, or scaling, of the reference VCSEL.

The comparison between the two-dimensional model and the reference VCSEL led to a number of inconsistent results. The most severe problem is that the predicted wavelength is 9850 Å, whereas the VCSEL operates at 9335 Å. For a laser, this is a huge error. Moreover, even if the cold cavity in the simulation is modified to match the experimental data, there is insufficient gain at 9335 Å to achieve startup. As a result, we cannot reconcile the modified simulation with the experimental data unless the energy gap for a strained-light-hole $In_xGa_{1-x}As$ quantum well [3] or the bandgap renormalization [4] is significantly in error. Another problem is that the two-dimensional model does not predict multiple modes, except when the laser intensity is sufficiently large to induce spatial hole burning. With spatial hole burning present, two modes separated by about 12 Å do appear in the intensity pattern. The first mode is Gaussian-like and the second mode is donut-like. Our conclusion is that the mode separation seen in the VCSEL is a dynamic effect, caused by spatial hole burning, rather than a cold-cavity effect.

These discrepancies between the two-dimensional model and the VCSEL data led to criticism against the two-dimensional field solver. As a result, we re-evaluated the utility of a three-dimensional model. It is not practical to solve a full three-dimensional coupled field-gain-transport model on a workstation. However, it is possible to solve the three-dimensional cold-cavity calculation on a workstation. A cold-cavity calculation determines the normal modes of a distributed VCSEL laser cavity with spatial variation in the dielectric and absorption coefficients, without a self-consistent active media model. So, rather than continue the development of the two-dimensional model, we developed a full three-dimensional cold-cavity model. The basic algorithm is the standard leap-frog used to solve Maxwell's equations,[5] but the equations are solved with a metric formulation to treat different coordinate systems.

The interesting aspect of the three-dimensional cold-cavity code is that the algorithm was implemented with a new technique based upon the Universal Interface (UI). The UI was developed in C++ upon a universal object called a fragment, which is a variable capable of representing all entities used in computing. The data structure, arithmetic functions, and I/O are all part of the fragment class interface. This universal structure enables code development to be accomplished simply as the direct

implementation of the equations in n-dimensional form. Boundary conditions were implemented for transmitting, periodic, and metallic boundaries. Field sources and material dielectric variations for the laser were implemented as a choice of point, distributed Gaussian, or eigenfunction solutions for a metal cavity.

The C++ functions describing the algorithm are simply hooked to the UI and run without change on machines of widely variable architecture and operating systems. The code has been run on Mac PowerBook540C, SUN4, HP735, IBM590 and CRAY-YMP platforms. The amount of code written is remarkably small and can be printed on three pages. Moreover, the performance of the code is excellent. The fragment solutions of Maxwell's equations run at a grind time of 0.23 μsec/cell/cycle and at a rate greater than 200 megaflops on the CRAY-YMP for three-dimensional problems.

The three-dimensional cold-cavity simulation for the reference VCSEL predicts a wavelength of about 9800 Å, consistent with the two-dimensional simulation. In addition, there is no evidence of higher order modes in the cold cavity. Thus, we are unable to explain the experimental data with either the two- or three-dimensional model. At this point, it is not clear if 1) the material coefficients are significantly incorrect, 2) some unknown physical effect is present in the experiment, or 3) the experimental data is incorrect.

In Sec. 2, a brief description of the reference VCSEL configuration is presented and the semi-empirical model connecting the lattice temperature and the carrier concentration is discussed. In Sec. 3, a brief description of the dielectric constant is given, including the modification due to lattice temperature and carrier concentration. In Sec. 4, the basic equations solved in the two-dimensional model are presented. In Sec. 5, some two-dimensional and three-dimensional results are presented.

2. CONFIGURATION AND SEMI-EMPIRICAL TRANSPORT MODEL

The two-dimensional simulation configuration for the reference VCSEL device is shown in Fig. 1. For this reference case, there are 80 regions along the z-direction, made up of 7 different materials. Along the x-axis, there are three major regions, separated by the horizontal lines shown in the figure. Only the center region contains active quantum wells; the positions of the quantum wells are indicated by the dark layer located about four-tenths of the distance along the z-axis. Both the lower and upper regions have increased absorption in the area around the quantum well region due to ion implantation, which effectively renders the quantum well layers inert. In the center region, the left-hand boundary is a metal, whereas in the lower and upper regions the left-hand boundary is a dielectric.

Starting from the left-hand boundary, there are a metal/dielectric layer, a phase matching layer, a 30-layer multi-layer-dielectric mirror, a cladding layer, three quantum well layers separated by four barrier layers, another cladding layer, a 37-layer multi-layer-dielectric mirror, a contact layer, and a coating layer. Although the longitudinal and transverse mesh sizes differ, both are uniform in space along either the longitudinal or transverse direction. Because this calculation uses a uniform mesh, it is necessary to slightly modify the index of refraction of some of the materials by a few percent. In addition, the transverse dimension of the simulation is much smaller than in an actual device, the simulation being limited to regions where the electric displacement is large. Except for these two assumptions, the simulation geometry is a very good representation of the actual reference VCSEL device.

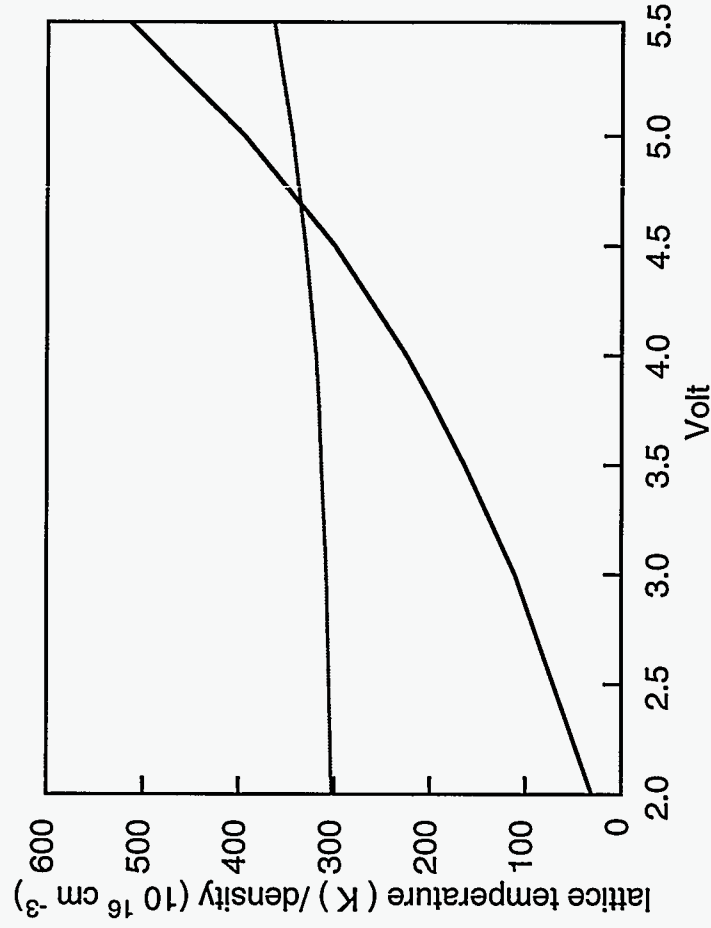Fig. 1. Two-dimensional simulation configuration for the reference VCSEL.

Fig. 2. The semi-empirical relationship between the concentration and lattice temperature as a function of the voltage applied to the VCSEL.

A semi-empirical model is used to connect the electron and hole concentrations with the lattice temperature. This semi-empirical relationship is shown in Fig. 2. In the figure, the line starting at 300 K and with the smaller slope is the lattice temperature. In the experiment, startup occurs at 3.8 V. This relationship impacts the details of the simulation. For example, if the carrier concentration is too low for the specified lattice temperature, startup is more difficult, the predicted wavelength is too low, and the rate of change of wavelength with voltage is too high.

3. INDEX OF REFRACTION MODEL

In the formulation of the field-gain model, one of the most fundamental assumptions concerns the bulk index of refraction. Although the active regions must be treated as a frequency dependent medium in the time domain, the model can be significantly simplified provided that the bulk index of refraction can be treated as frequency independent. The justification for this approximation is shown in Fig. 3, where the index of refraction of AlAs, $Al_{0.2}Ga_{0.8}As$, and GaAs are given as functions of wavelength.[6] AlAs has the lowest index of refraction. Now, the bandwidth of the laser is roughly given by the collisional dephasing time, which is $\Delta\lambda \approx 0.3$ μm. Referring to the figure, the change in the bulk index of refraction over this range is quite small. Thus, the bulk index of refraction is assumed to be frequency independent. In addition, the bulk absorption coefficient is assumed to be frequency independent.

Even though the bulk index of refraction is frequency independent, the index must be chosen to match the wavelength of operation of the device. Since the change in the index of refraction with wavelength is small, we make an initial guess for the operation wavelength, calculate the index from a semi-empirical model, and then perform a short calculation to determine the longitudinal mode wavelength. Based upon the calculation, the index is then modified slightly to provide an improved match.

For the reference VCSEL design, the bulk index of refraction is shown in Fig. 4. The data corresponds to a slice along the axis of the simulation. At the left-hand boundary, the zero index of refraction corresponds to a metal region. The wavelength varies significantly throughout the laser as the index of refraction varies over just a few wavelengths. This rapid variation in the index of refraction along the axis of the device implies that Maxwell's equations must be solved to obtain the field solution.

In addition to the variation of the bulk index of refraction, the index of refraction is slightly modified by the lattice temperature and carrier concentration. This modification is typically small. For example, near threshold, the contribution to the dielectric constant due to temperature and concentration is shown in Fig. 5. Again, the data corresponds to a slice along the axis of the simulation.

Combining the bulk, temperature, and carrier contributions, the dielectric constant is given by

$$\varepsilon = \left[n_{bulk} + \beta_{temp}(T - 300) \right]^2 + \chi_{den}, \tag{1}$$

where n_{bulk} is the material index of refraction, β_{temp} is the thermal coefficient for the index of refraction, and χ_{den} is the carrier concentration susceptibility. The carrier susceptibility is given by

$$\chi_{den} = -\frac{\omega_p^2}{\omega^2} \tag{2}$$

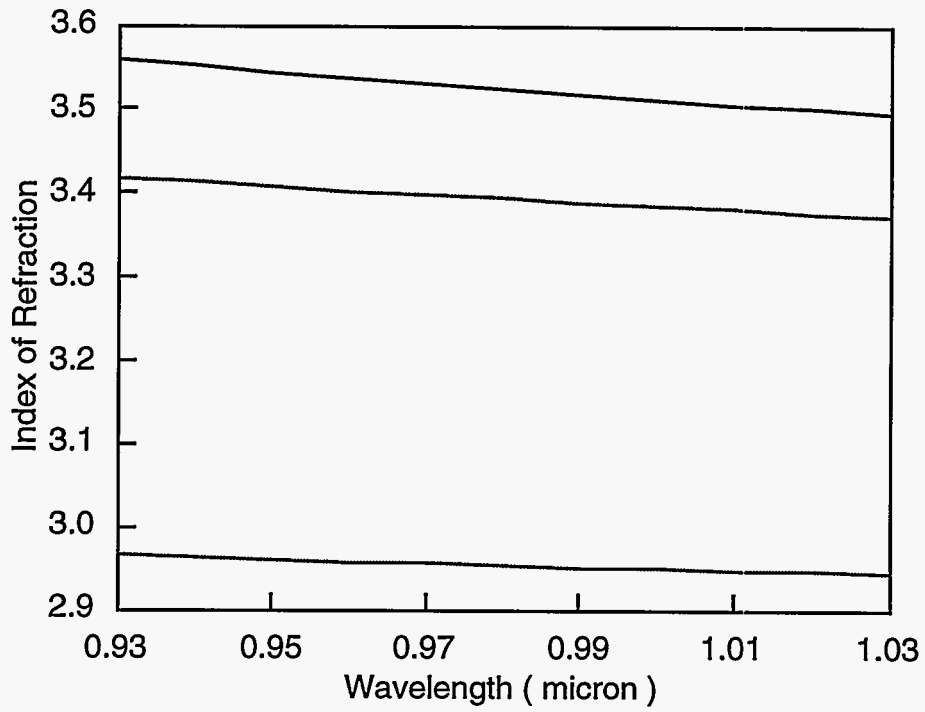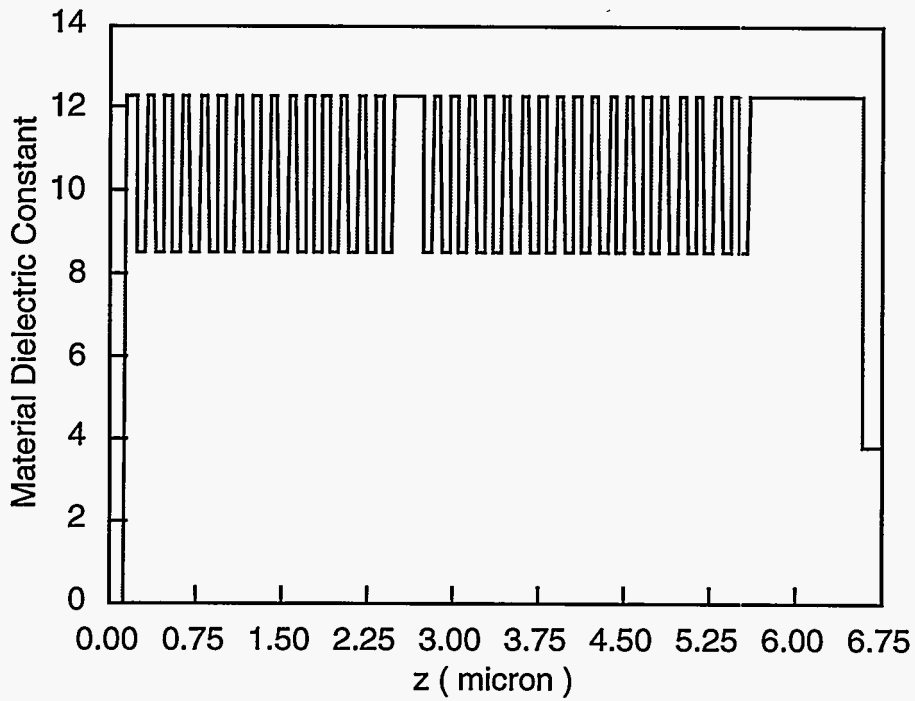Fig. 3. Semi-empirical index of refraction for GaAs, $Al_{0.2}Ga_{0.8}As$, and AlAs.

Fig. 4. Material contribution to the dielectric constant along the axis of the VCSEL.

in the bulk regions, and by

$$\chi_{den} = \frac{\omega_p^2}{\omega_{gap}^2 - \omega^2} \qquad (3)$$

in the quantum well regions. Here, ω_p is the plasma frequency calculated with a reduced mass, ω_{gap} is the bandgap frequency, and ω is the laser frequency. Note that $\beta_{temp} > 0$ and that $\chi_{den} < 0$, since $\omega_{gap} < \omega$. Thus, the change of index of refraction with temperature and concentration oppose one another.
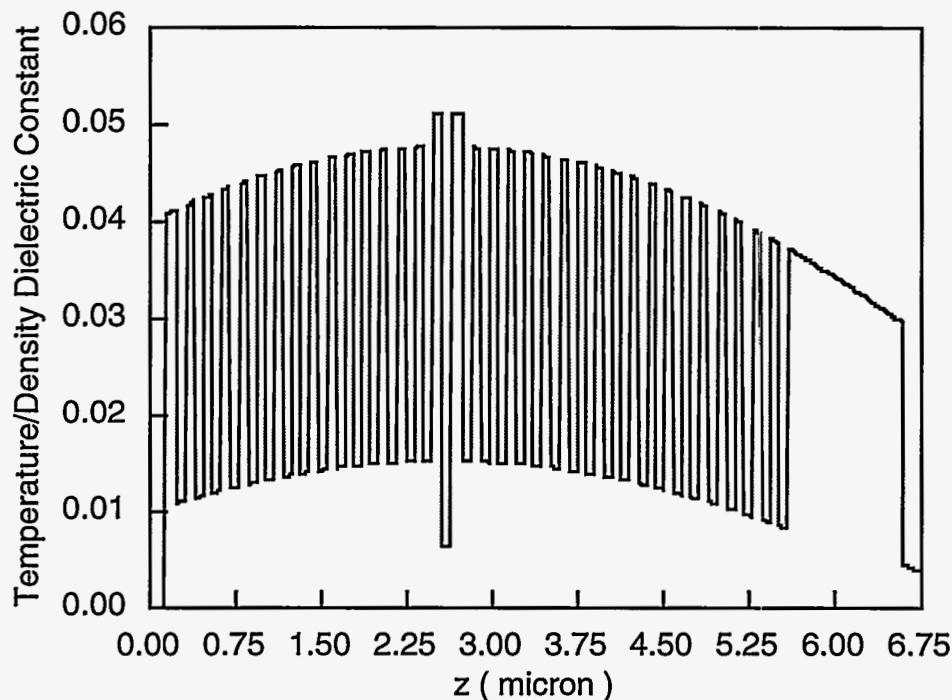

Fig. 5. Lattice temperature and carrier density modification to the dielectric constant along a slice down the axis of the VCSEL.

4. DIMENSIONLESS TWO-DIMENSIONAL MODEL EQUATIONS

Maxwell's equations are

$$\frac{\partial \mathbf{B}}{\partial t} = -\nabla \times \mathbf{E} \qquad (4)$$

and

$$\frac{\partial \mathbf{D}}{\partial t} = \nabla \times \mathbf{B} - \alpha \mathbf{D} + \frac{\partial \mathbf{P}}{\partial t}, \qquad (5)$$

where $\mathbf{D} = \varepsilon_0 n^2 \mathbf{E}$, n is the frequency-independent bulk index of refraction, α is the frequency-independent absorption coefficient, and $\mathbf{P}$ is the polarization vector associated with the active quantum

well regions. The polarization is related to the sine-like, P_s, and cosine-like, P_c, scalar polarization components, the time-dependent transition frequency $\omega_k(t)$, the dephasing collision frequency γ_k, and the dipole matrix element $\mathbf{d}$,

$$\mathbf{P} = \mathbf{d}\left[\omega_k(t)P_s - \gamma_k P_c\right]. \tag{6}$$

The scalar polarization components evolve according to

$$\frac{\partial P_c}{\partial t} = -\gamma_k P_c + \omega_k(t)P_s \tag{7}$$

and

$$\frac{\partial P_c}{\partial t} = 2\Omega \cdot \mathbf{D}n_h\Gamma(k) - \gamma_k P_s + \omega_k(t)P_c, \tag{8}$$

where Ω is the Rabi frequency, n_h is the hole concentration, and $\Gamma(k)$ is the fraction of the electron-hole pairs that contribute to the interaction. The quantity $\Gamma(k)$ is determined from an integration over k-space using Fermi-Dirac statistics. Here, k refers to the effective wave energy above the bandedge, determined from the difference between the transition frequency and the bandgap frequency. The bandgap frequency is calculated from a strained-quantum-well energy gap model, modified by lattice temperature, finite quantum well, and renormalization contributions. The time-dependent transition frequency, $\omega_k(t)$, is determined self-consistently from solution of Maxwell's equations.

Finally, the quantum well transport is given by

$$\frac{\partial n_e}{\partial t} = \nabla \cdot \mathbf{J}_e - \gamma_{nr}n_e - \Omega \cdot \mathbf{D}P_s \tag{9}$$

and

$$\frac{\partial n_h}{\partial t} = -\nabla \cdot \mathbf{J}_h - \gamma_{nr}n_h - \Omega \cdot \mathbf{D}P_s, \tag{10}$$

where $\mathbf{J}_e$ and $\mathbf{J}_h$ are the electron and hole current densities, respectively, and γ_{nr} is a concentration dependent loss term associated with nonradiative recombination and spontaneous emission. The bulk electron and hole contributions drive the longitudinal part of the divergence, $\partial J / \partial z$, while the transverse part of the divergence, $\partial J / \partial x$, leads to diffusion within the quantum well.

5. TWO-DIMENSIONAL AND THREE-DIMENSIONAL RESULTS

5.1. Two-dimensional results

The dependence of wavelength on lattice temperature is shown in Fig. 6. In the figure, simulation results are indicated by squares and experimental results by circles. The line passing through each data set is a linear fit used to determine the slope. First, the slope of both curves is positive, indicating that the change in the dielectric constant due to lattice temperature is dominating the change due to carrier

concentration. From the simulation, the predicted slope is $d\lambda / dT = 1.095$ Å/K. In contrast, the experimental data exhibits a slope of $d\lambda / dT = 0.695$ Å/K. Considering the sensitivity of the this slope calculation, the agreement is reasonable. Second, the predicted and observed magnitudes of the wavelengths are in disagreement by about 5%. For a laser, this is a huge error. We do not understand the source of this error in the wavelength prediction.
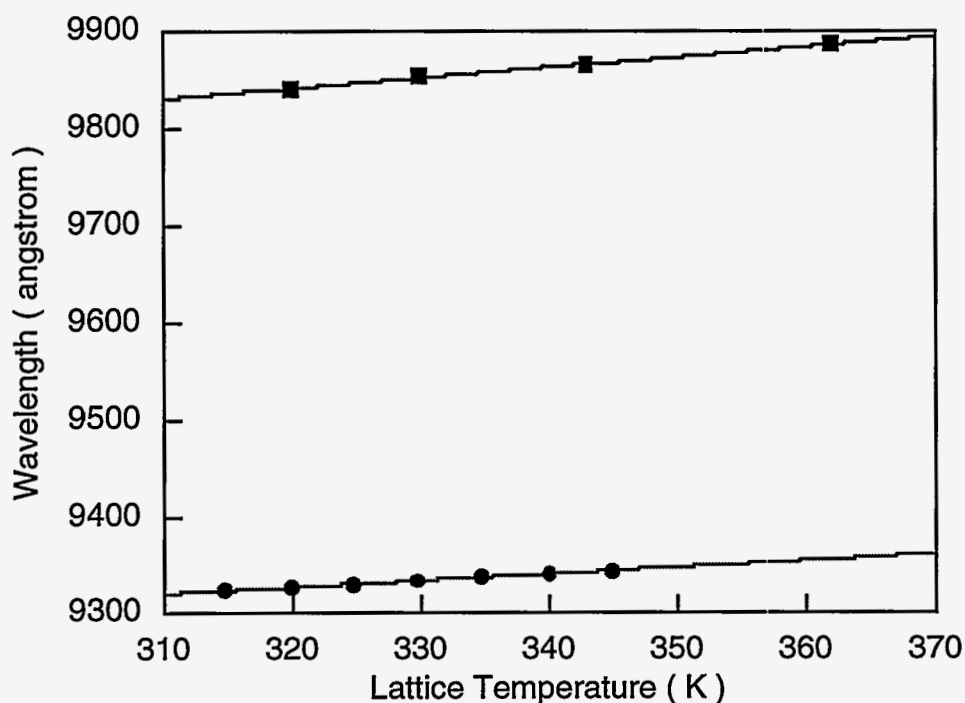

Fig. 6. Comparison of simulation and experimental wavelengths as a function of lattice temperature.

For conditions near threshold, the calculated gain for the reference VCSEL is given as a function of energy above the bandedge, see Fig. 7. Starting from the left, the three arrows indicate the position in energy space associated with 1) the reference configuration without bandgap renormalization, 2) the reference configuration with bandgap renormalization, and 3) a modified reference configuration forced to match the experiment. The first case starts up and saturates at a power level consistent with the experiment. The second case exhibits a very marginal startup and the saturated power is very small compared with the experiment. Finally, the third case, which corresponds to the experimental wavelength, is very far from startup. In short, even if we force the simulation to match the experimental wavelength, there is insufficient gain to ever start up, unless the strained-quantum-well-bandgap model [3] is significantly in error.

Finally, in Fig. 8, the Fourier transform of the electric field is shown over three different time intervals. The simulation corresponds to a drive condition significantly above threshold. Early in time (bottom curve) there is a single peak corresponding to a cold-cavity situation. Later in time (middle curve) the field has grown to sufficient amplitude to cause a phase shift to shorter wavelength. After saturation (top curve) two modes appear with a separation of 12 Å. The mode separation appears only after significant spatial hole burning appears. The predicted separation is in good agreement with the 10 Å seen in the experiment.
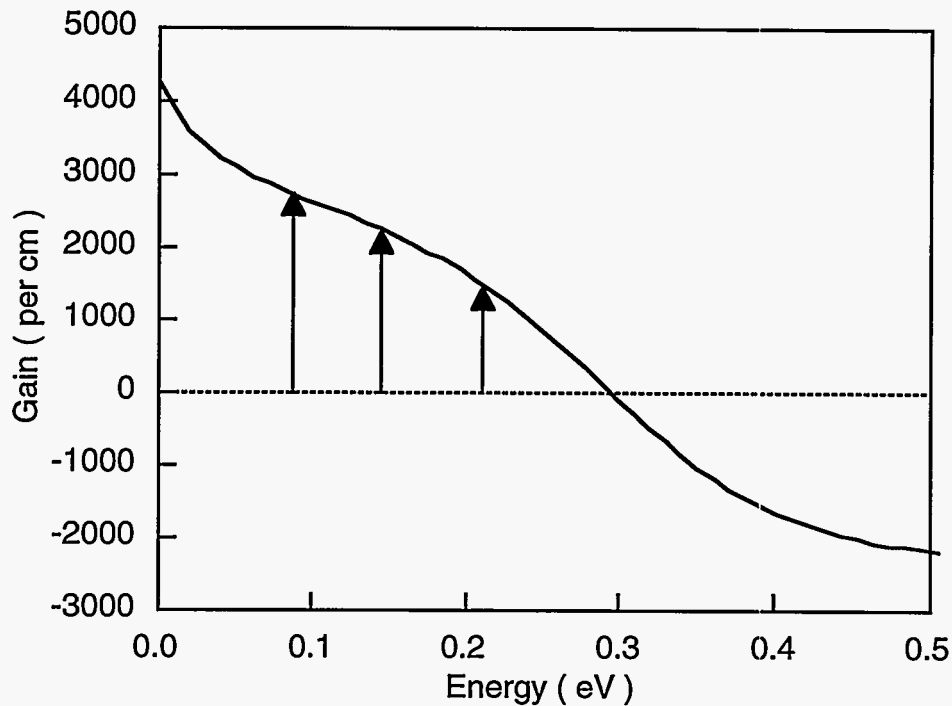
Fig. 7. Gain as a function of energy above the bandedge.

5.2. Three-dimensional results

As a test problem, we simulated a dielectric-filled metal box of length 6.75 μm, with equal transverse dimensions ranging from 2 μm to 8 μm. This problem has an analytic solution, and the effects of zoning are easily investigated. If the field solver is driven with both the correct eigenfunction and eigenfrequency, the simulation and analytic solution agree to within about 0.5%, provided there are 10 or more cells per wavelength. For the basic eigenfunctions, the separation between the eigenfrequencies is not constant.

A more interesting solution is obtained when the field solver is driven with an azimuthally-symmetric Gaussian-like source. In this case, we observe a number of equally spaced modes, the number of modes limited by the zoning of a particular simulation. For example, the Fourier transform of a simulation with a transverse dimension of 4 μm is shown in Fig. 9.

It is straight-forward to calculate that the mode spacing is about 35 Å for this case. If the three-dimensional system is driven at the frequency of one the peaks in the Fourier spectrum, it is possible to isolate a single pure mode. For example, driving at the frequency of the third mode shown in Fig. 9, produces the intensity pattern displayed in Fig. 10. The four bright spots in the pattern correspond to an $\ell = 4$ mode.
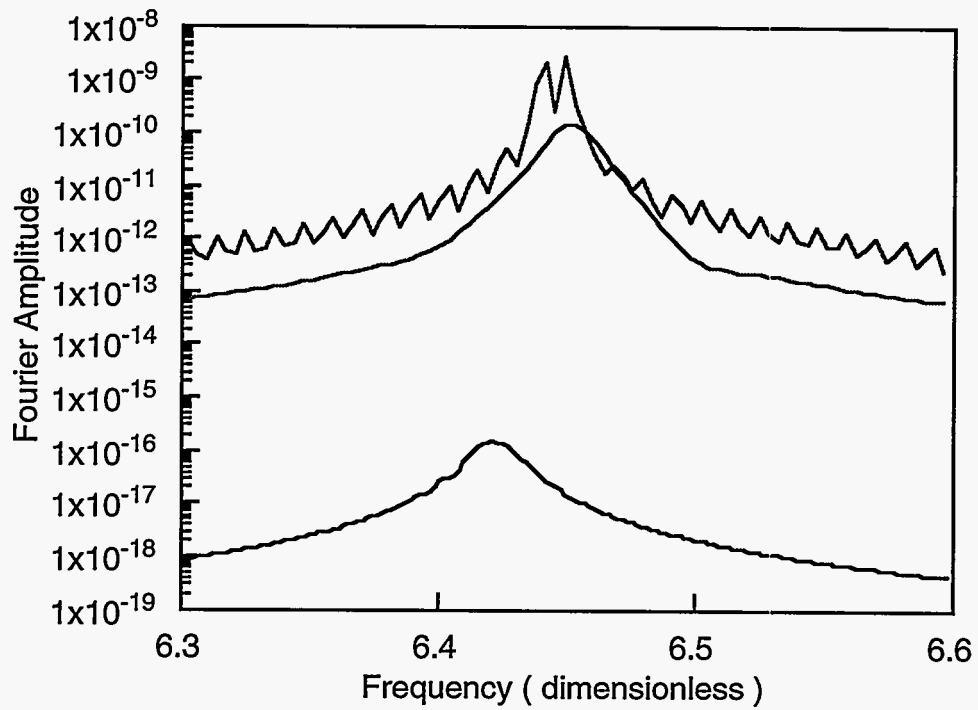
Fig. 8. Fourier transform of electric field at startup, exponential growth, and saturation.
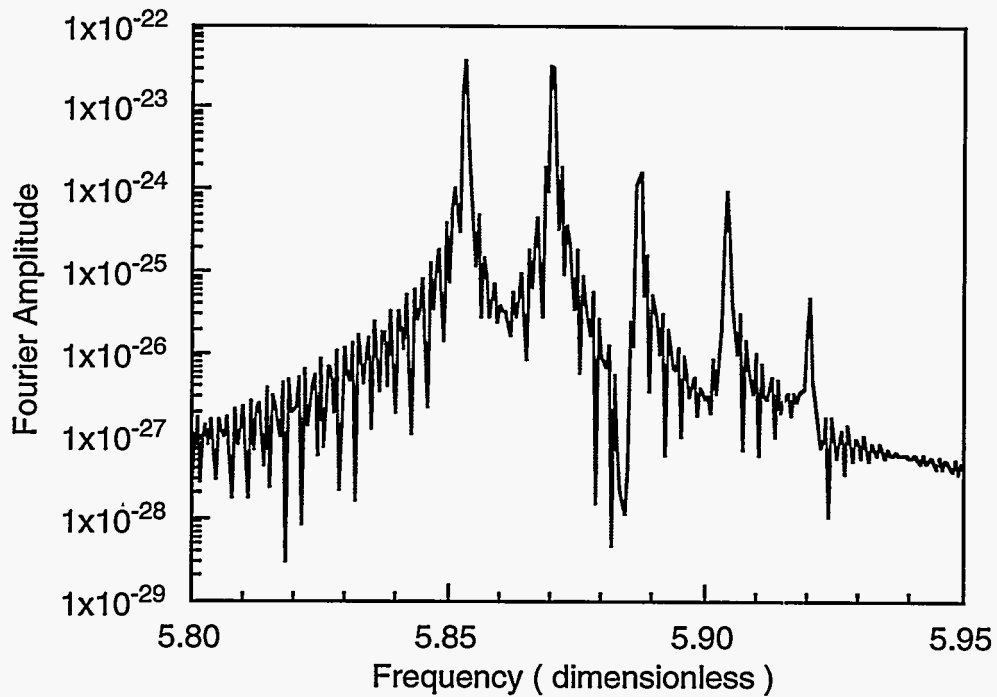

Fig. 9. Fourier transform of the electric field near the center of the metal box, showing five equally-spaced modes.
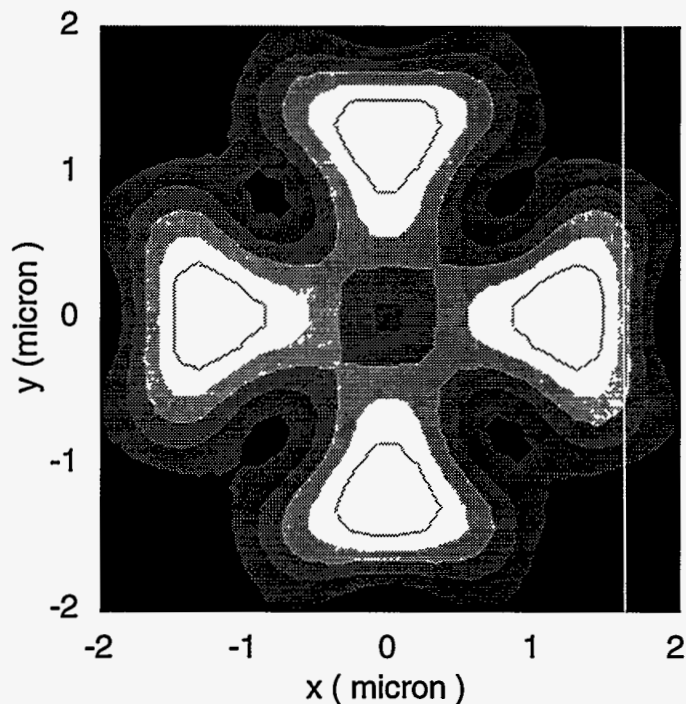
Fig. 10. The third mode intensity pattern perpendicular to the axis of the box.

We find the mode spacing obeys $L^2\Delta\omega \approx \text{constant}$, where L is the transverse dimension of the box. At $L = 8\ \mu\text{m}$, the mode spacing is less than 10 Å. Thus, we are able to observe transverse modes down to the level seen in the experiment. However, the scaling of the mode separation is not consistent with the experimental results, in which $L\Delta\omega \approx \text{constant}$. In the experiment, L is the diameter of the gain region. Because of the difference in scaling, we do not believe that the mode spacing seen in the experiment is due to a radial boundary effect, but is consistent with spatial hole burning.

6. ACKNOWLEDGMENTS

7. REFERENCES

1. Mike Tan, Hewlett-Packard Company, Private Communication.
2. L. E. Thode, G. Csanak, L. L. So, and T. J. T. Kwan, "Time-dependent numerical simulation of vertical cavity lasers," SPIE **2146**, 174 ,1994.
3. S. W. Corzine, R. H. Yan, and L. A. Coldren, "Optical gain in III-V bulk and quantum well semiconductors," in **Quantum Well Lasers**, edited by Peter S. Zory, Jr. (Academic Press, San Diego, 1993).
4. W. W. Chow, S. W. Koch, and M. Sargent III, **Semiconductor-Laser Physics** (Springer-Verlag, Berlin, 1994), p. 168.
5. M. N. O. Sadiku, **Numerical Techniques in Electromagnetics** (CRC Press, Boca Raton, 1992), p. 179.
6. M. A. Afromowitz, "Refractive Index of $Ga_{1-x}Al_xAs$," Solid State Commun. **15**, 59, 1974.